J. Fluid Mech. (1998), *vol.* 356, *pp.* 327–352. Printed in the United Kingdom

Analysis and modelling of subgrid-scale motions in near-wall turbulence

By CARLOS HÄRTEL† AND LEONHARD KLEISER†

DLR, Institute for Fluid Mechanics, Bunsenstr. 10, D-37073 Göttingen, Germany

(Received 19 July 1996 and in revised form 19 August 1997)

A numerical study of turbulent channel flow at various Reynolds numbers ($Re_\tau = 115$, 210, 300) is conducted in order to examine the requirements for a reliable subgrid modelling in large-eddy simulations of wall-bounded flows. Using direct numerical simulation data, the interactions between large and small scales in the near-wall flow are analysed in detail which sheds light on the origin of the inverse cascade of turbulent kinetic energy observed in the buffer layer. It is shown that the correlation of the wall-normal subgrid stress and the wall-normal derivative of the streamwise grid-scale velocity plays the key role in the occurrence of the inverse cascade. A brief *a priori* test of several subgrid models shows that currently applied models are not capable of accounting properly for the complex interactions in the near-wall flow. A series of large-eddy simulations gives evidence that this deficiency may cause significant errors in important global quantities of the flow such as the mean wall shear stress. A study of the eddy-viscosity ansatz is conducted which reveals that the characteristic scales usually employed for the definition of the eddy viscosity are inappropriate in the vicinity of a wall. Therefore, a novel definition of the eddy viscosity is derived from the analysis of the near-wall energy budget. This new definition, which employs the wall-normal subgrid stress as a characteristic scale, is more consistent with the near-wall physics. No significant Reynolds-number effects are encountered in the present analysis which suggests that the findings may be generalized to flows at higher Reynolds numbers.

1. Introduction

During the past two decades the large-eddy simulation (LES) technique has established its role as a powerful research tool for the study of turbulent flows in geophysics and engineering (see e.g. Galperin & Orszag 1993 or Härtel 1996 for more recent reviews of the field). In LES the flow-geometry-dependent large-scale (grid-scale, GS) motions are explicitly computed, while the small-scale (subgrid-scale, SGS) turbulence is accounted for by a model.

In developing subgrid models it is typically assumed that the SGS turbulence is in a state of approximate local isotropy. Consequently, the application of LES has been particularly successful in the study of free shear flows and turbulence at high Reynolds numbers, where approximate local isotropy often prevails. Currently large-eddy simulation is widely utilized for the analysis and prediction of geophysical flow phenomena; on the other hand, its use for engineering-type applications is still very

† Present address: Institute of Fluid Dynamics, Swiss Federal Institute of Technology, CH-8092 Zürich, Switzerland.

limited because engineering flows often exhibit a number of complicating features like solid walls, moderate Reynolds numbers and more complex flow geometries.

The key difficulties with the LES of wall-bounded flows originate in the presence of a wall layer in which viscosity plays a major role and in which locally significant turbulence structures may become extremely small. Essentially two different approaches exist to treat this wall layer in a LES. In the first approach, which in practice is the more common one, it is attempted to circumvent the very costly resolution of the near-wall turbulence structures by bridging the wall region with the aid of empirical boundary conditions for the outer layer (cf. Deardorff 1970; Schumann 1975; Piomelli, Ferziger & Moin 1989). These empirical boundary conditions correspond to the wall functions often applied in statistical turbulence simulations. In the second approach a refined mesh is employed in the vicinity of solid boundaries in order to resolve at least coarsely the most dominant near-wall structures. In general, no further empirical information about the near-wall flow is required in this approach. For high-Reynolds-number flows the application of approximate boundary conditions appears to be the only feasible way to treat the wall layer in a LES. It must be emphasized, however, that the near-wall turbulence structures may strongly influence the entire flow field, and that it is hence desirable to treat them more accurately whenever possible. More recently, Balaras & Benocci (1994) developed a new method for the near-wall treatment which takes an intermediate position between the two approaches outlined above. In their method a simplified set of equations, derived from the two-dimensional boundary-layer equations, is solved on an embedded grid between the wall and the first mesh point of the LES grid.

To develop subgrid models suitable for application in the highly inhomogeneous wall layer, detailed knowledge of the prevailing physical mechanisms in this flow regime is required. In this respect, the analysis of direct numerical simulation (DNS) data has made considerable contributions in recent years (cf. Domaradzki *et al.* 1994; Härtel *et al.* 1994; Horiuti 1993; Piomelli *et al.* 1989). An explicit filtering of the DNS results provides the required GS and SGS velocity and pressure fields, from which all further quantities of interest can be directly computed. A unique feature of DNS data is that they allow SGS models to be examined prior to their implementation by comparing exact and modelled SGS quantities for the same filtered flow field. A comparison of this type is usually termed an *a priori* test.

It has frequently been suggested that the key role of the subgrid model is to provide an exchange of energy between GS and SGS turbulence at roughly the correct rate (Rogallo & Moin 1984). Instantaneously, the flux of energy between resolved and unresolved scales is strongly intermittent, meaning that both the forward transfer from larger to smaller eddies and the reverse transfer often termed 'backscatter' can be encountered (cf. Domaradzki, Rogallo & Wray 1990; Piomelli *et al.* 1991). However, on the average energy is usually assumed to be transferred from larger to smaller scales which corresponds to the classical concept of an energy cascade. Since in this case the smaller scales essentially act as a sink of energy for the larger ones, they may efficiently be modelled by a dissipative eddy-viscosity ansatz on which virtually all current SGS models are based. The picture of an energy cascade is valid for most free flows, but cannot be applied to near-wall turbulence as was pointed out by Härtel *et al.* (1994). Analysing DNS data of turbulent channel and pipe flows the authors found that an inverse cascade of turbulent kinetic energy occurs in the buffer layer. The magnitude of this inverse transfer is very sensitive to the cutoff wavenumber, but it was found to depend little on the shape of the filter applied (Härtel & Kleiser 1997).

The present paper deals with the LES of wall-bounded turbulent flows and addresses several questions raised by the study of Härtel *et al.* (1994). Among other things the Reynolds-number dependence of their earlier findings is a major point of concern. Two new direct simulations of turbulent channel flow were performed and analysed during the course of the present study, one of them having a lower ($Re_\tau = 115$) and the other one a higher Reynolds number ($Re_\tau = 300$) than the flows considered by Härtel *et al.* (1994). After the governing equations have been laid out in §2, the relevant parameters of these simulations will be given in §3 along with a brief discussion of the numerical method. In §4 we present results of an analysis of the near-wall energy budget which is more comprehensive than previous ones. Subsequently in §5 the near-wall performance of three common subgrid models is examined by *a priori* tests and a series of large-eddy simulations. A more fundamental investigation of the eddy-viscosity ansatz will then be conducted in §6 where 'exact' DNS information is used to evaluate the characteristic scales from which the eddy viscosity is computed. A summary of our results together with some concluding remarks is given in §7.

2. Governing equations

In LES any dependent flow variable f is divided into a GS part $\bar{f}$ and a SGS part f', i.e. $f = \bar{f} + f'$. The definition of $\bar{f}$ can be based on a spatial filtering performed by convolving f with a filter function H (Leonard 1974):

$$\bar{f}(x_1, x_2, x_3, t) = \int_D \prod_{i=1}^{3} H_i(x_i - x_i', \Delta_i)\, f(x_1', x_2', x_3', t)\, \mathrm{d}x_1'\, \mathrm{d}x_2'\, \mathrm{d}x_3'. \tag{1}$$

The integration in (1) is extended over the whole domain D, and H_i denotes the filter function in the ith direction. Several suitable filter functions have been suggested in the literature, the most widely used ones among them being the Gaussian filter, the box filter, and the cutoff filter in spectral space. In the present study the spectral cutoff filter H_i^c has been used, which can conveniently be described by its Fourier transform $\hat{H}_i^c$:

$$\hat{H}_i^c(k_i) = \begin{cases} 1 & \text{for } |k_i| \leqslant K_i^c = 2\pi/\Delta_i \\ 0 & \text{otherwise,} \end{cases} \tag{2}$$

where k_i designates the wavenumber. In (1) and (2) Δ_i is the width of the filter in the ith direction and K_i^c denotes the cutoff wavenumber.

A different splitting of the flow variables, which will also be employed here, is the Reynolds decomposition, where a quantity g is split into a statistical mean value $\langle g \rangle$ and a fluctuation $\tilde{g}$, i.e.

$$g = \langle g \rangle + \tilde{g}. \tag{3}$$

Whenever the operator $\langle \cdot \rangle$ is used here, it symbolizes an averaging over the wall-parallel planes of the channel, the two channel halves, and all stored time levels of the DNS. Such averages are subsequently referred to as global averages.

Filtering the continuity and Navier–Stokes equations yields the evolution equations for the large scales. For an incompressible fluid of constant density ϱ and constant viscosity they read

$$\frac{\partial \bar{u}_k}{\partial x_k} = 0, \tag{4}$$

$$\frac{\partial \bar{u}_i}{\partial t} + \frac{\partial}{\partial x_k}(\overline{\bar{u}_i \bar{u}_k}) = -\frac{\partial \bar{p}}{\partial x_i} + \frac{\partial Q_{ik}}{\partial x_k} + \nu \frac{\partial^2 \bar{u}_i}{\partial x_k \partial x_k}. \tag{5}$$

In (4) and (5) u_i denotes the velocity component in the ith direction, p the pressure, ν the kinematic viscosity of the fluid, and the usual tensor notation is employed. The effect of the unresolved scales appears in the SGS stress tensor Q_{ij} which consists of two contributions

$$Q_{ij} = C_{ij} + R_{ij}, \tag{6}$$

where

$$C_{ij} = -(\overline{\bar{u}_i u'_j} + \overline{u'_i \bar{u}_j}), \quad R_{ij} = -\overline{u'_i u'_j}. \tag{7}$$

C_{ij} and R_{ij} are usually termed SGS cross-stresses and SGS Reynolds stresses, respectively.

For the temporal evolution of each component of the stress tensor Q_{ij} a budget equation can be derived from the filtered and unfiltered equations of motion:

$$\frac{\partial Q_{ij}}{\partial t} = \sum_{l=1}^{6} T_l^{ij}, \tag{8}$$

with the individual terms T_l^{ij} given by

$$\left.\begin{aligned}
T_1^{ij} &= -\overline{\bar{u}_k \frac{\partial Q_{ij}}{\partial x_k}} - \overline{\bar{u}_k \frac{\partial L_{ij}}{\partial x_k}}, \\
T_2^{ij} &= \frac{\partial}{\partial x_k}(\overline{u_i u_j u_k} - \overline{\bar{u}_i \bar{u}_j \bar{u}_k} - \overline{\bar{u}_j \bar{u}_i \bar{u}_k} - \overline{\bar{u}_k \bar{u}_i \bar{u}_j} + 2\overline{\bar{u}_i \bar{u}_j \bar{u}_k}), \\
T_3^{ij} &= \frac{\partial}{\partial x_i}(\overline{p u_j} - \overline{\bar{p}\bar{u}_j}) + \frac{\partial}{\partial x_j}(\overline{p u_i} - \overline{\bar{p}\bar{u}_i}) - \overline{p\left(\frac{\partial u_i}{\partial x_j} + \frac{\partial u_j}{\partial x_i}\right)} + \overline{\bar{p}\left(\frac{\partial \bar{u}_i}{\partial x_j} + \frac{\partial \bar{u}_j}{\partial x_i}\right)}, \\
T_4^{ij} &= -\left(\overline{Q_{ik}\frac{\partial \bar{u}_j}{\partial x_k}} + \overline{Q_{jk}\frac{\partial \bar{u}_i}{\partial x_k}}\right) - \left(\overline{L_{ik}\frac{\partial \bar{u}_j}{\partial x_k}} + \overline{L_{jk}\frac{\partial \bar{u}_i}{\partial x_k}}\right), \\
T_5^{ij} &= \nu \frac{\partial^2 Q_{ij}}{\partial x_k \partial x_k}, \\
T_6^{ij} &= 2\nu\left(\overline{\frac{\partial u_i}{\partial x_k}\frac{\partial u_j}{\partial x_k}} - \overline{\frac{\partial \bar{u}_i}{\partial x_k}\frac{\partial \bar{u}_j}{\partial x_k}}\right).
\end{aligned}\right\} \tag{9}$$

The term $L_{ij} = \overline{\bar{u}_i \bar{u}_j} - \bar{u}_i \bar{u}_j$ in (9) denotes the so-called Leonard stresses (Leonard 1974) which are a function of the GS velocities only.

The budget equation for the kinetic energy of the GS motions $E^{GS} = (\bar{u}_k \bar{u}_k)/2$ is obtained by multiplying the filtered Navier–Stokes equations by the GS velocity $\bar{u}_i$. In this equation the effect of the SGS motions on the energy balance of the resolved flow field is given by the term

$$\bar{u}_k \frac{\partial Q_{kl}}{\partial x_l} = \frac{\partial}{\partial x_l}(\bar{u}_k Q_{kl}) - Q_{kl}\bar{S}_{kl}, \tag{10}$$

where $\bar{S}_{ij}$ denotes the GS rate-of-strain tensor

$$\bar{S}_{ij} = \frac{1}{2}\left(\frac{\partial \bar{u}_i}{\partial x_j} + \frac{\partial \bar{u}_j}{\partial x_i}\right). \tag{11}$$

The first term on the right-hand side of (10) accounts for a spatial redistribution of GS kinetic energy due to SGS motions. The second term $Q_{kl}\bar{S}_{kl}$ governs the exchange of energy between GS and SGS turbulence, and is usually called 'SGS dissipation'.

Positive values of the SGS dissipation indicate a flux of kinetic energy from large to small scales, whereas the transfer is reversed whenever it takes negative sign. In this paper we will concentrate on the global average of the SGS dissipation which is designated as ε hereafter, i.e.

$$\varepsilon = \langle Q_{kl}\bar{S}_{kl}\rangle. \tag{12}$$

By application of (3) the global average of the SGS dissipation may be decomposed into two parts, one of them being due to mean (MS) and the other due to fluctuating rates of strain (FS), respectively (Härtel *et al.* 1994):

$$\varepsilon = \langle Q_{kl}\rangle\langle\bar{S}_{kl}\rangle + \langle\tilde{Q}_{kl}\tilde{\bar{S}}_{kl}\rangle = \varepsilon^{MS} + \varepsilon^{FS}. \tag{13}$$

In (13) the term $\varepsilon^{MS} = \langle Q_{kl}\rangle\langle\bar{S}_{kl}\rangle$ means an enhancement of SGS turbulence in the presence of mean-flow gradients. The second term $\varepsilon^{FS} = \langle\tilde{Q}_{kl}\tilde{\bar{S}}_{kl}\rangle$ accounts for a redistribution of energy within the turbulence spectrum without affecting the mean flow directly. An individual analysis of the terms ε^{MS} and ε^{FS} provides a more detailed insight into the energy budget of the flow than can be obtained from considering their sum only.

Since the current study is concerned with the LES of near-wall flows, most of the results will be given in common wall units, i.e. normalized by the friction velocity $u_\tau = (\tau_w/\rho)^{1/2}$ (τ_w denotes the wall shear stress) and ν, which are the appropriate reference quantities for wall turbulence. Any quantity scaled in wall units will be indicated by the usual superscript $+$.

3. DNS databases

For the present analysis we primarily employed a DNS database of turbulent channel flow at a wall Reynolds number of about $Re_\tau = 210$ (based on friction velocity u_τ and channel half-width h). The simulation was performed by Gilbert & Kleiser (1991) and the results have been validated carefully by comparison with other simulations and recent experimental results. This simulation, denoted as simulation II (SII) in the following, falls within the range of low Reynolds numbers where a universal scaling of flow quantities in wall units cannot yet be expected (cf. Antonia & Kim 1994; Wei & Willmarth 1989). Therefore, we conducted two further DNS, one of them having a lower and the other a higher Reynolds number than simulation II. These DNS will subsequently be referred to as simulation I and simulation III (SI and SIII). The respective Reynolds numbers are $Re_\tau = 115$ and $Re_\tau = 300$. A comparison of results obtained from the three databases should reveal whether significant Reynolds-number effects exist.

3.1. *Numerical method*

The flow domain and the coordinate system used in the simulations are illustrated in figure 1, where x_1 denotes the streamwise, x_2 the spanwise, and x_3 the normal direction. The respective lengths of the computational domain related to the channel half-width h differ for the three simulations and were chosen such that the dominant correlation lengths of the turbulence fields can be accommodated. For the simulations at $Re_\tau = 210$ and 300 these correlation lengths are governed by the dynamics of the large eddies in the core flow; for the smallest Reynolds number, on the other hand, the elongated near-wall structures are more relevant. All simulations were conducted with a constant mass flux Q. As initial condition, a laminar Poiseuille flow was employed in SII with superimposed small-amplitude disturbances which trigger the transition to

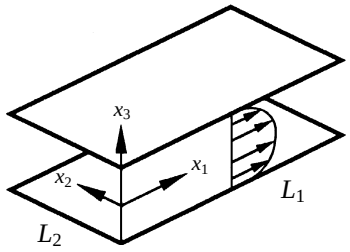

FIGURE 1. Computational domain and coordinate system.

	Simulation I	Simulation II	Simulation III
Re_{CL}	1973	3831	5662
Re_Q	1667	3333	5000
Re_τ	115	210	300
Geometry	$24h \times 12h \times 2h$	$11.22h \times 5.98h \times 2h$	$12h \times 6h \times 2h$
Grid	$200 \times 160 \times 64$	$160 \times 160 \times 128$	$250 \times 240 \times 192$
Δx_1^+	13.7	14.8	14.4
Δx_2^+	8.6	7.9	7.5
$(\Delta x_3^+)_{min}$	0.138	0.064	0.04
$(\Delta x_3^+)_{max}$	5.60	5.18	4.91
T_{sim}^+	1174	980	612
N_T	45	22	17
ΔT^+	26.7	46.7	38.3

TABLE 1. Parameters of the DNS of turbulent channel flow. Re_{CL}: Reynolds number based on channel-centreline velocity, Re_Q: Reynolds number based on bulk velocity, Re_τ: Reynolds number based on friction velocity, T_{sim}: total time span of the simulation, N_T: number of permanently stored time layers, ΔT: time span between two successive stored time layers.

turbulence. Simulations I and III were initialized with fully turbulent flow fields taken from SII. In all cases data were assembled only after the first transient phase had passed and a statistically stationary state was attained. The relevant parameters of the three DNS such as the discretization and the total time span T_{sim} of the simulation are given in table 1. The time span T_{sim} does not include the initial transients. Also given in the table is the number N_T of permanently stored time layers of each simulation along with the time span ΔT between two successive time layers. In all cases ΔT is sufficiently large to make sure that each two successive time layers of a simulation are essentially statistically independent.

The numerical scheme used is based on a fully spectral spatial discretization with Fourier expansions in the wall-parallel directions and Chebyshev polynomials in x_3 (see Kleiser & Schumann 1984). The time discretization is done in a semi-implicit manner where an explicit method is employed for the nonlinear terms together with a Crank–Nicolson scheme for the viscous terms and the pressure. In SII an Adams–Bashforth method was utilized for the explicit part, while a third-order-accurate Runge–Kutta scheme was applied in SI and SIII. The evaluation of the nonlinear terms is done pseudospectrally. To eliminate aliasing errors, the 3/2 rule (see Canuto *et al.* 1988) was applied in all three directions in SI and SII. In SIII, where no full dealiasing could be performed owing to limited computational resources, the 3/2 rule was applied in the spanwise direction only.

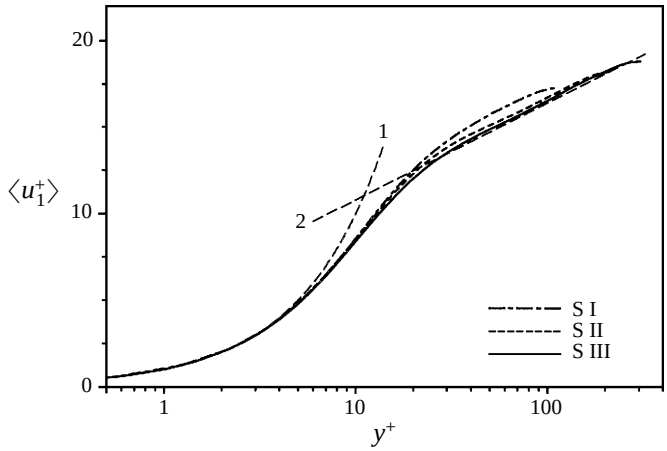

FIGURE 2. Mean-velocity profiles of turbulent channel flow in wall units. Results of three direct numerical simulations at different Reynolds numbers. $Re_\tau = 115$ (SI), 210 (SII), and 300 (SIII). Curve 1: $\langle u_1^+ \rangle = y^+$, curve 2: $\langle u_1^+ \rangle = 2.44 \ln y^+ + 5.17$ (Dean 1978).

3.2. *Mean-velocity profiles*

For a brief comparison of the three direct simulations, the respective mean-velocity profiles are displayed on a semi-logarithmic scale in figure 2 (see Härtel 1994 for a more detailed assessment). Here and in what follows the wall distance y will generally be used rather than the wall-normal coordinate x_3. All of the velocity profiles exhibit the characteristic linear increase within the viscous sublayer ($y^+ \leqslant 5$), but a marked logarithmic regime can be discerned for the two higher Reynolds numbers only. The universal logarithmic law of the wall according to Dean (1978)

$$\langle u_1 \rangle^+ = 2.44 \ln y^+ + 5.17, \tag{14}$$

has been included in the figure for comparison, which makes it obvious that the profile of SIII is already very close to the experimentally established high-Reynolds-number law.

4. Analysis of the turbulent energy budget

The SGS effects in a turbulent flow depend qualitatively and quantitatively on the width of the filter function applied. Generally speaking, the filter width should be as large as possible in order to minimize the computational needs of a simulation, but larger filter widths give rise to a more complex SGS turbulence which puts higher demands on the subgrid models. If a considerable fraction of the kinetic energy resides in the small scales, the SGS turbulence will contain structures which play an important role in the whole turbulence dynamics. Therefore, judicious guidelines are needed for the spatial resolution which ensure that important features like the evolution of near-wall streaks or bursts can be captured by the numerical grid. Zang (1991) suggested grid spacings of about $\Delta x_1^+ = 80$ in the streamwise and $\Delta x_2^+ = 30$ in the perpendicular wall-parallel direction. This corresponds approximately to the following cutoff wavenumbers of the cutoff filter (2):

$$(K_1^c)^+ = 0.039, \quad (K_2^c)^+ = 0.104. \tag{15}$$

According to current practice in LES (see e.g. Härtel *et al.* 1994; Piomelli 1993),

	Simulation I	Simulation II	Simulation III
$(K_1^c)^+ = 2\pi/\Delta_1^+$	0.041	0.042	0.042
$(K_2^c)^+ = 2\pi/\Delta_2^+$	0.083	0.08	0.083

TABLE 2. Cutoff wavenumbers used in the filtering of the DNS databases (Δ_i is the filter width in the ith direction). K_1^c: streamwise direction, K_2^c: spanwise direction. Wavenumbers given in wall units.

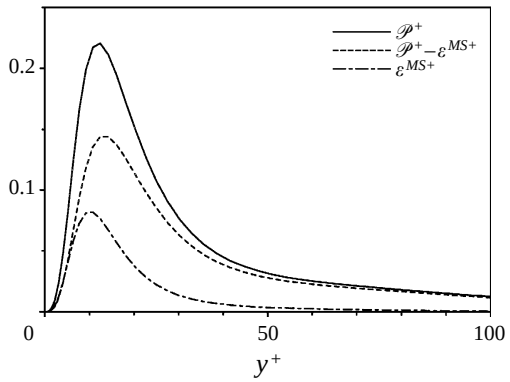

FIGURE 3. Total turbulence production $\mathscr{P}$ and its components $\mathscr{P} - \varepsilon^{MS}$ and ε^{MS} due to grid-scale and subgrid-scale turbulence, respectively. Results for simulation II.

a resolution of $\Delta x_2^+ = 30$ appears to be the upper limit, while in the streamwise direction a much coarser resolution may still suffice. The filter widths used in the present analysis are summarized in table 2. No filtering was performed in the normal direction x_3, since in this direction a rather fine resolution is required to resolve the steep mean-flow gradients. This implies that in our case the following equalities hold:

$$\langle g \rangle = \overline{\langle g \rangle} = \langle \bar{g} \rangle. \tag{16}$$

Furthermore, since we employ a spectral cutoff filter,

$$\langle C_{ij} \rangle = 0, \quad \text{i.e.} \quad \langle Q_{ij} \rangle = \langle R_{ij} \rangle. \tag{17}$$

If the filter widths (15) are employed, the SGS turbulence will still contain dynamically significant turbulence structures in the near-wall region below $y^+ = 30$, say. The relative importance of GS and SGS turbulence is illustrated by figure 3, where the common turbulence production $\mathscr{P}$

$$\mathscr{P} = \langle u_k u_l \rangle \langle S_{kl} \rangle = \langle \bar{u}_k \bar{u}_l \rangle \langle S_{kl} \rangle + \langle u_l' u_k' \rangle \langle S_{kl} \rangle \tag{18}$$

and its respective contributions due to resolved and unresolved motions are depicted. The second equality in (18) holds by virtue of (16) and (17). Moreover, it can be shown with the aid of (16) and (17) that the contribution of the unresolved motions $\langle u_l' u_k' \rangle \langle S_{kl} \rangle$ is identical to ε^{MS} in the present case. Figure 3 illustrates that the SGS turbulence is of minor importance with respect to the turbulence production in the core flow, but plays a significant role close to the walls. In the very near-wall region ($y^+ < 10$ in figure 3) GS and SGS turbulence contribute almost equally to $\mathscr{P}$. This

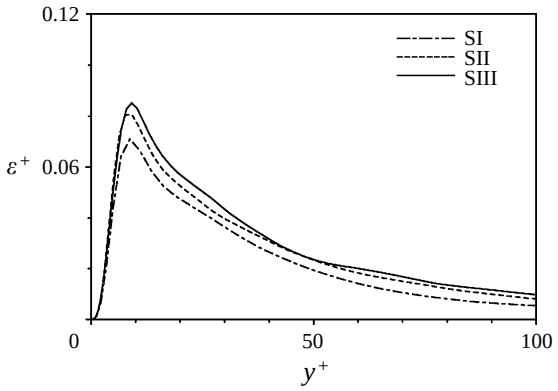

FIGURE 4. SGS dissipation ε. Comparison of results for different Reynolds numbers.

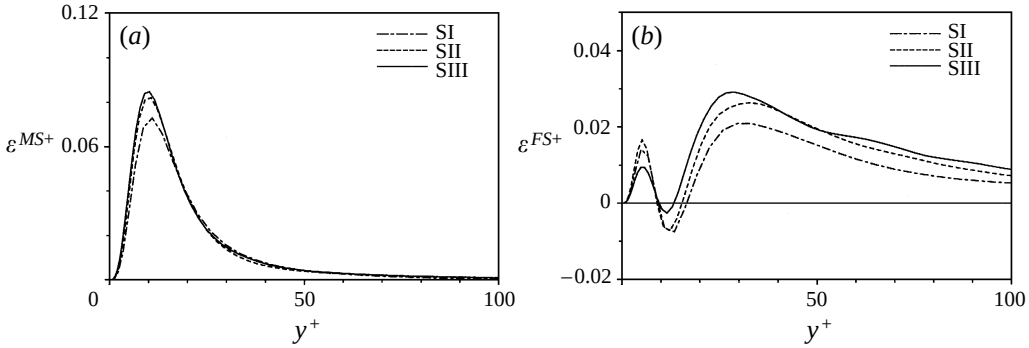

FIGURE 5. SGS dissipation ε^{MS} due to mean rates of strain (*a*) and ε^{FS} due to fluctuating rates of strain (*b*). Comparison of results for different Reynolds numbers.

makes clear why the near-wall flow is particularly sensitive to an accurate SGS modelling.

4.1. *SGS dissipation*

Figure 4 shows the global averages of the SGS dissipation as computed from the DNS databases using the cutoff wavenumbers given in table 2. Results are displayed for the region $y^+ \leqslant 100$ which amounts to one third of the channel half-width h in SIII, but essentially equals h in SI. From the figure it is seen that ε increases slightly with Re, while being qualitatively almost independent of Reynolds number. In all cases the SGS dissipation is non-negative throughout the channel, meaning that on the average the net transfer of kinetic energy is from GS to SGS motions.

The individual components ε^{MS} and ε^{FS} of the SGS dissipation are given in figure 5. Again a good agreement in the results for the different Reynolds numbers is seen. The quantitative differences in the results are somewhat more pronounced for ε^{FS} than for ε^{MS}. However, in all cases ε^{FS} exhibits a marked kink within the buffer layer ($5 \leqslant y^+ \leqslant 30$) and attains negative values which indicate the reverse flux of kinetic energy already observed by Härtel *et al.* (1994). Figure 5 shows that this important characteristic of the wall layer is only little affected by the Reynolds number. The slight quantitative differences observed probably have little significance: since the magnitude of the inverse transfer is very sensitive to the cutoff wavenumber K_2^c (Härtel *et al.* 1994), changes in K_2^c of a few percent may result in changes in ε^{FS}

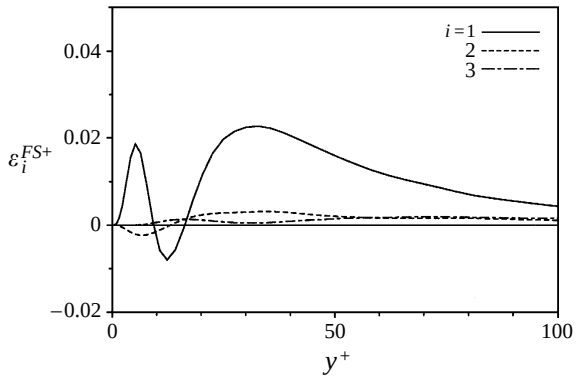

FIGURE 6. Splitting of ε^{FS} into three contributions ε_i^{FS} from the budget equations for $\langle\tilde{\tilde{u}}_i\tilde{\tilde{u}}_i\rangle/2$ (no summation). Definition of ε_i^{FS} according to (20). Results for simulation II.

which are of the same order of magnitude as the differences between the results for the different Reynolds numbers seen in figure 5.

To elucidate the origin of the reverse energy cascade in more detail, we analysed the relevant energy transfer terms. The main results are presented in the following. In a first step we examined which of the GS velocity components $\tilde{\tilde{u}}_i$ are predominantly affected by the inverse cascade. To this end the exchange terms ε_i^{FS} which enter the three budget equations were evaluated for the individual components of the GS turbulent kinetic energy $\langle\tilde{\tilde{u}}_i\tilde{\tilde{u}}_i\rangle/2$ (no summation):

$$\varepsilon_i^{FS} = \langle\tilde{Q}_{ik}\,\partial\tilde{\tilde{u}}_j/\partial x_k\rangle \quad (j = i). \tag{19}$$

Results for ε_i^{FS}, obtained from SII, are given in figure 6. It is seen that the exchange of GS and SGS kinetic energy acts almost exclusively on the velocity component $\tilde{\tilde{u}}_1$ in the streamwise direction, while the spanwise and wall-normal velocities play a marginal role. The sharp kink within the buffer layer, observed in the curve for ε_1^{FS}, clearly corresponds to the kink in ε^{FS} discussed above. Decomposing ε_1^{FS} into its components due to Q_{11}, Q_{12} and Q_{13}, respectively, reveals that the reverse transfer is primarily caused by the stress component Q_{13}, i.e. the subgrid stress aligned with the mean rate of strain. The contribution of Q_{13} to ε_1^{FS}, hereafter denoted by $\varepsilon_{1,13}^{FS}$,

$$\varepsilon_{1,13}^{FS} = \langle\tilde{Q}_{13}\partial\tilde{\tilde{u}}_1/\partial x_3\rangle, \tag{20}$$

is shown in figure 7, where the pronounced negative minimum in the buffer layer becomes obvious.

For the further analysis we will now consider the evolution equation for $\varepsilon_{1,13}^{FS}$. This equation is obtained by differentiating $\varepsilon_{1,13}^{FS}$ with respect to time which yields

$$\frac{\partial}{\partial t}\varepsilon_{1,13}^{FS} = \left\langle\frac{\partial\tilde{Q}_{13}}{\partial t}\frac{\partial\tilde{\tilde{u}}_1}{\partial x_3}\right\rangle + \left\langle\tilde{Q}_{13}\frac{\partial}{\partial t}\frac{\partial\tilde{\tilde{u}}_1}{\partial x_3}\right\rangle. \tag{21}$$

The required time derivative of Q_{13} is given by (8), while the time derivative of $\partial\tilde{\tilde{u}}_1/\partial x_3$ is obtained by differentiating the x_1-momentum balance with respect to x_3. We have evaluated both terms on the right-hand side of (21), but results will only be shown here for the first term which we found to be more revealing concerning the

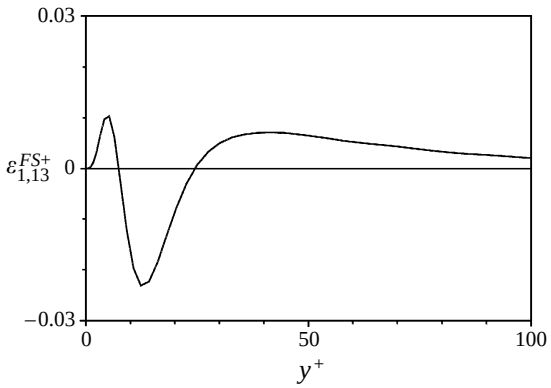

FIGURE 7. Contribution of the SGS stress component Q_{13} to ε_1^{FS}. Results for simulation II.

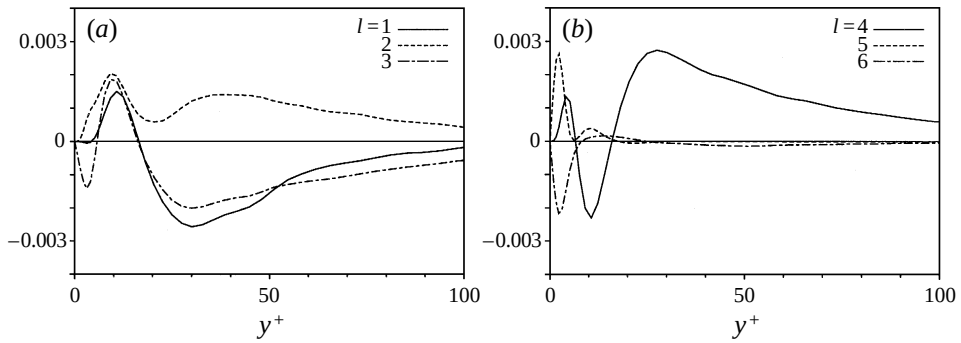

FIGURE 8. Global averages of the terms $\tilde{T}_l^{13}\,\partial\tilde{\tilde{u}}_1/\partial x_3$ (see equation (8)) from the budget equation $\partial/\partial t\left\langle \tilde{Q}_{13}\,\partial\tilde{\tilde{u}}_1/\partial x_3\right\rangle$. Results for simulation II.

origin of the inverse transfer. Using (8) it can be written as

$$\left\langle \frac{\partial\tilde{Q}_{13}}{\partial t}\frac{\partial\tilde{\tilde{u}}_1}{\partial x_3}\right\rangle = \sum_{l=1}^{6}\left\langle \tilde{T}_l^{13}\frac{\partial\tilde{\tilde{u}}_1}{\partial x_3}\right\rangle. \tag{22}$$

The results for the six individual terms on the right-hand side of (22) are summarized in figure 8. For $l = 1, 4$ the contributions due to the Leonard stresses L_{ij}, which are a function of the GS flow field only, have been excluded. From the figure it is seen that the viscous diffusion and viscous dissipation ($l = 5$, 6) play an important role in the immediate vicinity of the wall, but may be neglected above the viscous sublayer. The remaining four terms, being comparable in magnitude, are significant throughout the channel. Regarding the origin of the reverse transfer of energy within the buffer layer, the results suggest that the production term $\tilde{T}_4^{13}$, which is roughly balanced by the pressure term $\tilde{T}_3^{13}$, plays a decisive role. Note that negative values of $\left\langle \tilde{T}_4^{13}\partial\tilde{\tilde{u}}_1/\partial x_3\right\rangle$ represent an enhancement of the reverse transfer due to $\varepsilon_{1,13}^{FS}$. Comparing figures 7 and 8 reveals that positive and negative signs of $\varepsilon_{1,13}^{FS}$ approximately coincide with positive and negative signs of $\left\langle \tilde{T}_4^{13}\tilde{\tilde{u}}_1/\partial x_3\right\rangle$.

From (9) it was seen that T_4^{13} consists of six individual terms (after excluding those containing L_{ij}), and hence $\left\langle \tilde{T}_4^{13}\,\tilde{\tilde{u}}_1/\partial x_3\right\rangle$ may be split into the corresponding six contributions for further analysis. The contributions of these six terms to $\left\langle \tilde{T}_4^{13}\,\partial\tilde{\tilde{u}}_1/\partial x_3\right\rangle$

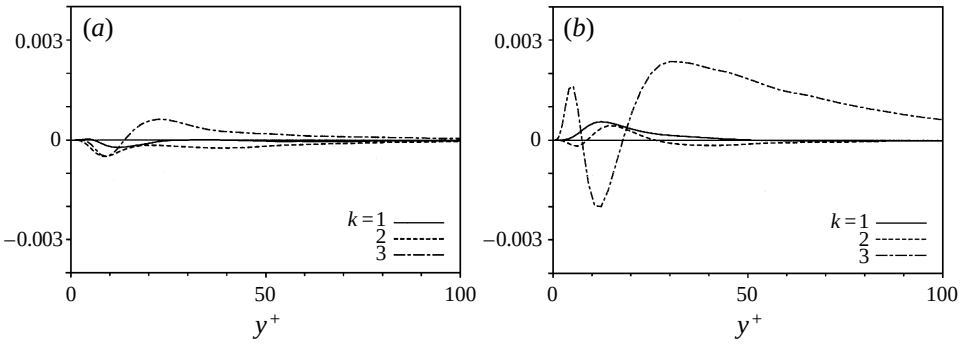

FIGURE 9. Contribution of the individual terms $-Q_{1k}\ \partial\bar{u}_3/\partial x_k$ (*a*) and $-Q_{3k}\,\partial\bar{u}_1/\partial x_k$ (*b*) to $\left\langle \tilde{T}_4^{13}\,\partial\tilde{u}_1/\partial x_3 \right\rangle$. Results for simulation II.

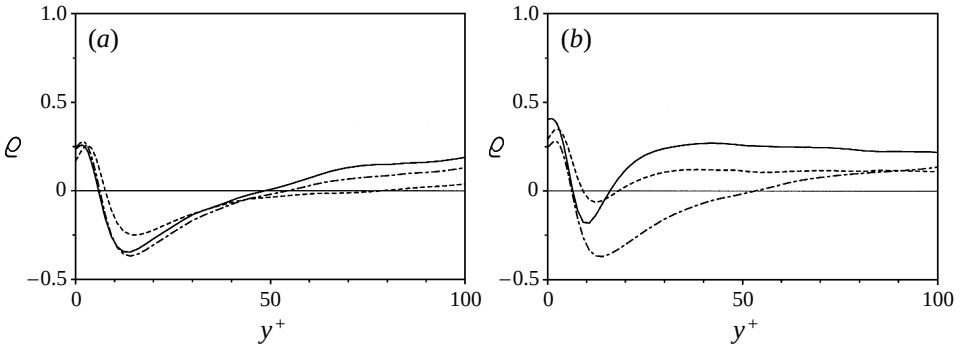

FIGURE 10. (*a*) Correlation coefficient between $\partial\tilde{u}_1/\partial x_3$ and $\tilde{R}_{33}$ (——), $\tilde{C}_{33}$ (- - - -) and $\tilde{Q}_{33}$ ($-\cdot-$). (*b*) Correlation coefficient ϱ between $\partial\tilde{u}_1/\partial x_3$ and $\tilde{Q}_{11}$ (——), $\tilde{Q}_{22}$ (- - - -) and $\tilde{Q}_{33}$ ($-\cdot-$). Results for simulation II.

are summarized in figure 9. As can be seen from the curves, the term $-Q_{33}\,\partial\bar{u}_1/\partial x_3$ is the dominant one throughout the channel and governs the sum $\left\langle \tilde{T}_4^{13}\,\tilde{u}_1/\partial x_3 \right\rangle$ completely. Since the covariance of fluctuations in $-Q_{33}\,\partial\bar{u}_1/\partial x_3$ and $\partial\bar{u}_1/\partial x_3$ is directly connected to the relation between the GS shear $\partial\bar{u}_1/\partial x_3$ and the wall-normal SGS stress Q_{33}, it may be inferred from the results in figure 9 that close to the wall a systematic phase shift prevails between the latter two quantities. This is illustrated more clearly by the respective correlation coefficient ϱ between $-Q_{33}$ and $\partial\bar{u}_1/\partial x_3$ shown in figure 10. The correlation coefficient ϱ of two fluctuating quantities f and g is defined in the usual way:

$$\varrho(\tilde{f},\tilde{g}) = \left\langle \tilde{f}\cdot\tilde{g} \right\rangle / \mathrm{rms}(\tilde{f})\cdot\mathrm{rms}(\tilde{g}), \tag{23}$$

where rms denotes the root-mean-square fluctuation. In figure 10 a region of negative correlation is seen which exhibits a minimum located well within the buffer layer and which extends much further into the core of the channel than did the negative parts in the other curves discussed above. For comparison, the correlation coefficients between $\partial\tilde{u}_1/\partial x_3$ and the negative of the two components $\tilde{R}_{33}$ and $\tilde{C}_{33}$ of $\tilde{Q}_{33}$ is included in the figure, giving evidence that concerning the correlation with $\partial\tilde{u}_1/\partial x_3$ no significant difference exists between the cross- and SGS Reynolds stresses. In figure 10(*b*) the correlation coefficient between $\partial\tilde{u}_1/\partial x_3$ and $-\tilde{Q}_{33}$ is compared with the corresponding correlation coefficients between $\partial\tilde{u}_1/\partial x_3$ and the negative of the

streamwise and spanwise SGS normal stresses $\tilde{Q}_{11}$ and $\tilde{Q}_{22}$, respectively. All three stresses exhibit a similar behaviour, but it is seen that the wall-normal stress Q_{33}, featuring the most extended region of negative correlation, plays a particular role. In §6 we will discuss how this finding may be exploited in order to derive a definition of the SGS eddy viscosity which is more consistent with the dominant features of near-wall turbulence than are the definitions usually applied.

5. Assessment of subgrid models

The analysis in the preceding section revealed the complicated structure of the interactions between GS and SGS motions in the near-wall region. Whether or not currently applied subgrid models are capable of taking proper account of these interactions will now be examined by an *a priori* test of three more widely applied models. One of these models, the Smagorinsky model, is then employed in a series of large-eddy simulations of turbulent channel flow at various Reynolds numbers.

All SGS models examined here are eddy-viscosity models, where the deviatoric part τ_{ij} of the SGS stress tensor Q_{ij} is set proportional to the rate-of-strain tensor $\bar{S}_{ij}$ of the resolved flow field:

$$\tau_{ij} := Q_{ij} - \delta_{ij} Q_{kk}/3 = 2 \nu_t \bar{S}_{ij}. \tag{24}$$

The closure problem is thus reduced to finding a (scalar) eddy viscosity ν_t as a function of the resolved flow variables. Before the results of the *a priori* test are discussed we will briefly introduce the three different models, but for more details the reader is referred to the literature cited below.

The first model is the classical Smagorinsky (1963) model, where the SGS eddy viscosity is derived under the assumption that the small-scale turbulence is locally in equilibrium regarding production and dissipation of kinetic energy. This leads to

$$\nu_t = (C_S \Delta x)^2 \, \|\bar{S}\| \quad \text{where} \quad \|\bar{S}\| = (2 \bar{S}_{kl} \bar{S}_{kl})^{1/2}. \tag{25}$$

In (25) the grid size of the computational mesh is denoted by Δx and C_S is a yet undetermined model constant, named the Smagorinsky constant. For homogeneous isotropic turbulence exhibiting an infinitely extended inertial range, Lilly (1967) analytically derived a value of $C_S = 0.17$ which, however, was found to be too large in practice. Therefore the more common value $C_S = 0.1$ will be used in the subsequent analysis (Deardorff 1970). Following Piomelli, Moin & Ferziger (1988) Δx is computed as the geometric mean of the mesh sizes in the three coordinate directions and the eddy viscosity is supplied with an additional Van Driest-type damping function (see Van Driest 1956) to ensure the proper near-wall behaviour $\nu_t \propto (y^+)^3$. This yields

$$\nu_t = C_S^2 \left[1 - \exp\left(-(y^+/A^+)^3\right)\right] (\Delta x_1 \Delta x_2 \Delta x_3)^{2/3} \, \|\bar{S}\|. \tag{26}$$

The constant A^+ in (26) is set to the common value $A^+ = 25$ here.

The second model is the structure-function model proposed by Métais & Lesieur (1992). Following Chollet & Lesieur (1981) the authors assumed that the proper SGS velocity scale, on which the eddy viscosity should be based, is given by the square-root of the kinetic energy residing at the cutoff wavenumber K^c. While Chollet & Lesieur defined the eddy viscosity in spectral space, Métais & Lesieur derived a physical-space representation of the model by resorting to the second-order velocity-structure function. Here we will use a two-dimensional version of this model, where the structure-function is computed from velocity differences taken in the wall-parallel planes (see Comte, Lee & Cabot 1990). To achieve an improved near-wall behaviour,

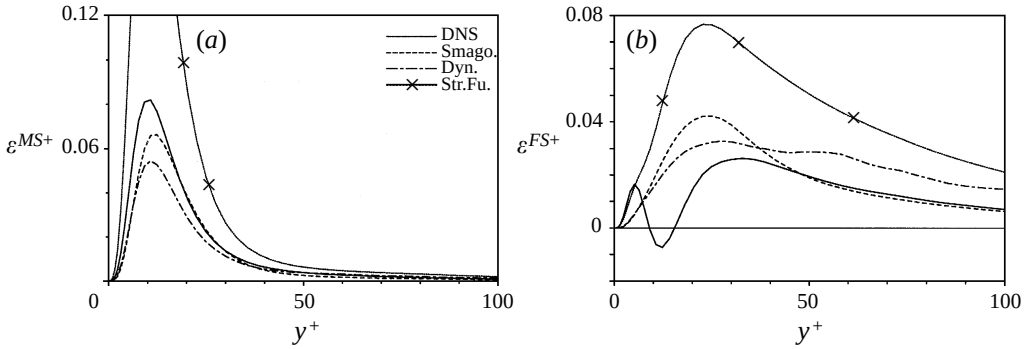

FIGURE 11. SGS dissipation ε^{MS} due to mean rates of strain (*a*) and ε^{FS} due to fluctuating rates of strain (*b*). Comparison of DNS results with various SGS models. Results for simulation II.

the resulting eddy viscosity is supplied with a wall-damping function $\mathrm{D}(y^+) = (1 - \exp(-y^+/25))^2$ (see Zang, Chang & Ng 1992).

The third model examined here is the dynamic Smagorinsky model suggested by Germano *et al.* (1991) and improved by Lilly (1992). In the dynamic Smagorinsky model C_S is no longer assumed to be constant, but is considered a function of space and time. This is motivated by the experience that the optimum value of the Smagorinsky constant may greatly vary from flow to flow, ranging between 0.07 and 0.24 (Rogallo & Moin 1984; Schumann 1991). It is hence desirable to avoid an *ad hoc* specification of the Smagorinsky constant by somehow adjusting C_S to the actual, local state of the flow. In the dynamic model this is achieved by introducing a second filter (the so-called 'test filter') in addition to the original LES filter. Assuming that the SGS stresses due to both the original filter and the test filter are similar and can be modelled using the identical ansatz, a relation for the evaluation of C_S can be derived. In the present study the model is employed in an averaged version, where C_S is taken as a function of time and the inhomogeneous coordinate x_3 only, while being constant within the homogeneous wall-parallel planes. A fully localized version of this model has also been devised, but was not found to be clearly superior to the averaged one in cases where directions of homogeneity are present in the flow (Ghosal *et al.* 1995).

5.1. A priori *test*

For the *a priori* test the models were applied to the filtered velocity fields of SII and the SGS dissipation was then evaluated with the modelled stresses. The respective results for ε^{MS} and ε^{FS} are shown in figure 11, along with the correct data obtained from the DNS. It is seen that the results for the structure-function model are significantly in excess of the DNS data, which confirms conclusions already arrived at by Comte *et al.* (1990). All models appear to give qualitatively satisfactory results with respect to ε^{MS}, but the curves for ε^{FS} reveal that none of them captures the inverse cascade of energy. Rather, the modelled transfer of energy within the turbulence spectrum is from GS to SGS motions throughout the channel. For all models ε^{FS} monotonically increases from the wall to a global maximum located at about $y^+ = 25$ which gives rise to significant differences between the modelled and correct dissipation over the whole buffer layer. Concerning the adjustment of C_S as implemented in the dynamic model used here, an interesting consequence can be drawn from figure 11. Since C_S was assumed to be a function of wall distance and time only, it does not affect

the correlation between SGS stresses and GS rates of strain within the wall-parallel planes. Therefore both ε^{MS} and ε^{FS} are directly proportional to C_S at each wall-normal position. Within the buffer layer the dynamically obtained values for C_S are clearly too large concerning ε^{FS}, but slightly too small concerning ε^{MS}. This shows that in the averaged version of the dynamic model the constant cannot be adjusted such that a satisfactory modelling of both ε^{MS} and ε^{FS} is achieved.

If one of the above models is employed in a LES, one may expect that the excessive values of the modelled dissipation ε^{FS} degrade the LES results within the buffer layer. This will probably affect the whole near-wall flow, since in the buffer layer the maximum production of turbulent kinetic energy occurs. Simultaneously, the transport of turbulence energy takes its negative extremum there, meaning that an excessive damping of turbulence cannot be compensated by additional wall-normal transport. Of crucial importance is the fact that the near-wall flow and the core flow are essentially decoupled by the logarithmic regime where turbulence is approximately in equilibrium, especially at high Reynolds numbers. Consequently, the quality of the simulation results in the outer flow should have little effect on the quality of the results in the near-wall region and vice versa. Whether or not these presumptions are confirmed by an *a posteriori* test, i.e. by actual large-eddy simulations, is examined in §5.2.

5.2. A posteriori *test*

For the *a posteriori* test we performed LES of turbulent channel flow for three bulk Reynolds numbers Re_Q identical to those of the direct simulations. The computational domains used for these LES were the same as those used for the DNS (see table 1), and the grid sizes in the spanwise and streamwise directions were chosen such that they approximately correspond to a filtering with the cutoff wavenumbers given in table 2. The corresponding discretizations used in the simulations are

$$\left.\begin{aligned} Re_Q = 1667: &\quad N_1 \times N_2 \times N_3 = 36 \times 36 \times 32, \\ Re_Q = 3333: &\quad N_1 \times N_2 \times N_3 = 32 \times 32 \times 64, \\ Re_Q = 5000: &\quad N_1 \times N_2 \times N_3 = 48 \times 48 \times 96. \end{aligned}\right\} \tag{27}$$

Since the *a priori* test did not reveal significant qualitative differences between the three subgrid models, only the Smagorinsky model was employed in the simulations. The numerical method used for the LES is essentially the same as the one used for the DNS and is described in Härtel (1994).

It was already noted that results of a LES with the Smagorinsky model (26) may depend considerably on the constant C_S. Therefore a proper choice of C_S is of primary importance. Before the LES were conducted, we determined an optimized value of C_S for the three different Reynolds numbers by requiring that the overall exchange of kinetic energy between GS and SGS motions should be represented correctly by the model. The corresponding optimization condition reads

$$\left\langle \tau_{kl}^{mod} \bar{S}_{kl} \right\rangle_{D,t} = \left\langle \tau_{kl}^{DNS} \bar{S}_{kl} \right\rangle_{D,t}, \tag{28}$$

where $\langle \cdot \rangle_{D,t}$ indicates an averaging over the whole computational domain and all time layers stored. The superscripts *mod* and *DNS* in (28) denote the modelled stresses and the stresses computed from the DNS data. The respective values of the optimized Smagorinsky constant, termed C_S^* hereafter, are given in table 3. The significance of C_S^* will become evident from the results presented below.

	$Re_Q = 1667$	$Re_Q = 3333$	$Re_Q = 5000$
C_S^*	0.078	0.100	0.114

TABLE 3. Energetically optimized Smagorinsky constant C_S^* for various Reynolds numbers Re_Q.

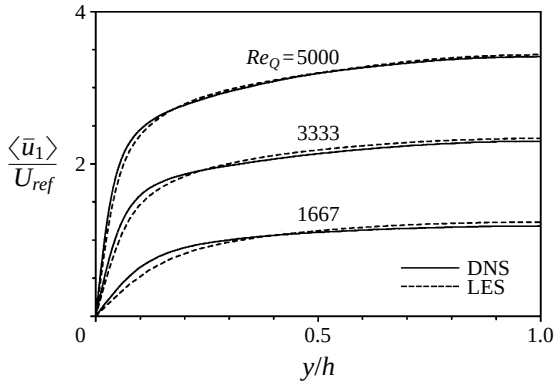

FIGURE 12. Mean-velocity profiles of turbulent channel flow. Comparison of DNS data with LES results at various bulk Reynolds numbers Re_Q. The bulk velocity u_Q of simulation I has been used as the reference velocity $\boldsymbol{U}_{ref}$ here. For each Reynolds number the mass flux is the same for DNS and LES. Model constants: $Re_Q = 1667, 3333$: $C_S = C_S^*$, $Re_Q = 5000$: $C_S = 0.96\, C_S^*$.

	$Re_Q = 1667$ $C_S = C_S^*$		$Re_Q = 3333$ $C_S = C_S^*$		$Re_Q = 5000$ $C_S = 0.96\, C_S^*$	
	Re_{CL}	Re_τ	Re_{CL}	Re_τ	Re_{CL}	Re_τ
DNS	1973	115	3831	210	5662	300
LES	2061	99	3890	189	5721	273
ε_{Re}	4.5%	14%	1.5%	10%	1%	9%

TABLE 4. Centreline Reynolds number Re_{CL} and wall Reynolds number Re_τ for DNS and LES. Results for various bulk Reynolds numbers Re_Q. The relative error in the LES results related to the DNS results is denoted by ε_{Re}.

5.2.1. *LES results for different Reynolds numbers*

In figure 12 the mean-velocity profiles of the direct simulations are displayed together with velocity profiles obtained from LES. For the two lower Reynolds numbers C_S was set to C_S^*, while for the highest Reynolds number C_S was set to a value slightly lower than the optimized one. The reason is that the latter LES was conducted with a guess for C_S^*, since the full DNS results were not yet available when the LES was performed. Note that the velocity profiles in figure 12 are not given in wall units, but were non-dimensionalized by the channel half-width h and the bulk velocity u_Q of SI (u_Q is the mass flux in x_1 divided by the density ρ and the channel cross-section). Like in the DNS, the mass flux Q was also prescribed in the LES, and consequently the bulk Reynolds numbers Re_Q are identical for DNS and LES. On the other hand, the centreline Reynolds numbers Re_{CL} and the wall Reynolds numbers Re_τ are free to fluctuate in time. The averages of these Reynolds numbers are given in table 4.

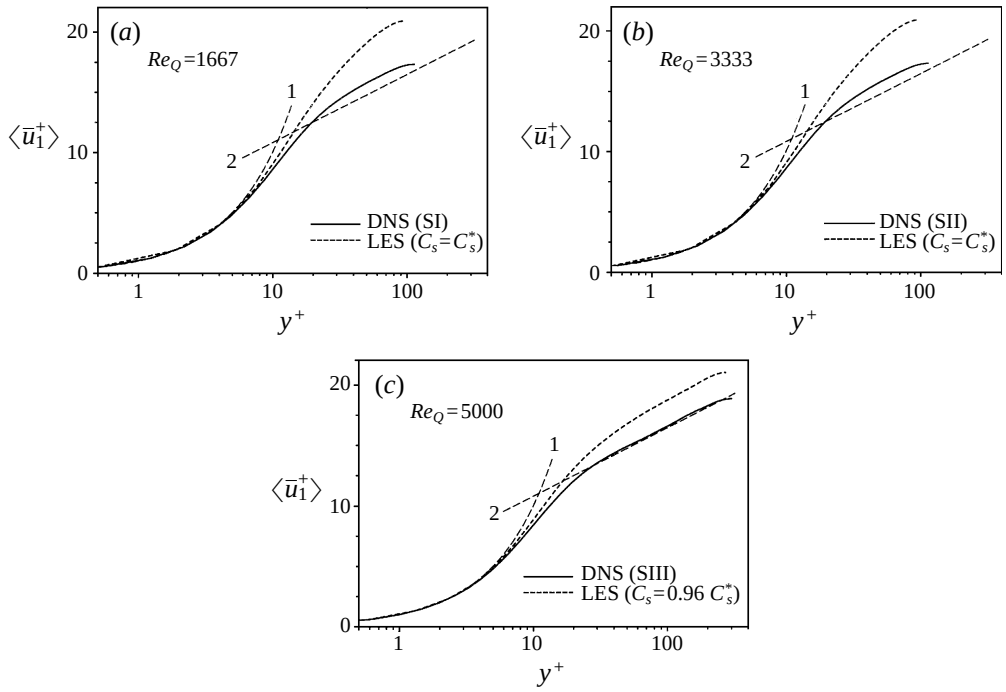

FIGURE 13. Mean-velocity profiles in wall units. Comparison of DNS and LES results for various Reynolds numbers. Curve 1: $\langle u_1^+ \rangle = y^+$, curve 2: $\langle u_1^+ \rangle = 2.44 \ln y^+ + 5.17$.

Figure 12 reveals that away from the wall the quality of the LES results improves significantly with increasing Reynolds number. This is confirmed by inspection of table 4, where the relative error in Re_{CL} is seen to decrease from about 5% for the lowest Reynolds number to approximately 1% for the highest one. This result is not surprising, since both theoretical considerations and practical experience suggest that within the outer flow the Smagorinsky model is a more efficient subgrid model at higher than at lower Reynolds numbers.

From figure 12 it appears that the errors in the LES results are generally larger in the near-wall region than in the core flow, as was to be expected from the *a priori* test. To quantify the errors in the wall layer more precisely, one may directly compare the resulting wall Reynolds numbers Re_τ of DNS and LES. From table 4 it is found that the relative error of the LES decreases from about 14% for $Re_Q = 1667$ to 9% for $Re_Q = 5000$, which indicates that these errors are much less reduced at higher Reynolds numbers than were those in Re_{CL}. Figure 13 gives the velocity profiles from figure 12 in wall units on a semi-logarithmic scale. Clearly, both DNS and LES correctly give a linear velocity profile below $y^+ \approx 5$, but above a wall distance of $y^+ \approx 10$ the curves for the DNS and the LES diverge significantly. Too large values are obtained from the LES, as a consequence of the discrepancies in the mean-velocity gradients at the wall. Figure 13 shows that for the LES a developed logarithmic range exists for $Re_Q = 5000$ only, while for the DNS it is clearly discernible for $Re_Q = 5000$ and 3333. The rather poor LES results for the two lower Reynolds numbers reflect the much stronger coupling between wall layer and core flow in these cases.

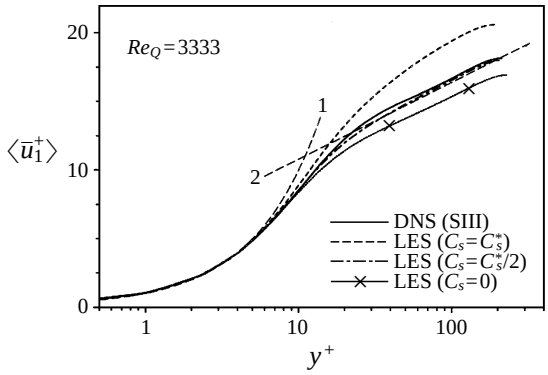

FIGURE 14. Mean-velocity profiles of turbulent channel flow in wall units. Comparison of DNS results with LES results for various values of the Smagorinsky constant C_S. Curve 1: $\langle u_1^+ \rangle = y^+$, curve 2: $\langle u_1^+ \rangle = 2.44 \ln y^+ + 5.17$.

5.2.2. *LES results for different values of C_S*

From the above results one might speculate that (28) is not the appropriate optimization of the Smagorinsky constant in the present case. Generally speaking, lower values of C_S should result in increased turbulence fluctuations and consequently in steeper velocity profiles at the wall. Conversely, higher values of C_S damp the resolved scales more strongly which can be expected to result in reduced wall gradients. To examine the effect of C_S, three series of LES with a systematic variation of C_S were conducted at the different bulk Reynolds numbers. As an example, figure 14 shows the resulting mean-velocity profiles of three of the simulations at $Re_Q = 3333$, where the model constant was set to $C_S = C_S^*$, $C_S = C_S^*/2$ and $C_S = 0$, respectively. Owing to the scaling used, all curves collapse in the viscous sublayer, but significant differences become visible beyond the lower edge of the buffer layer. The simulation with $C_S = 0$ (i.e. with no model at all) exhibits a developed logarithmic regime with the correct slope, but the velocities are considerably below the DNS curve throughout. This illustrates that too steep wall gradients result if no subgrid model is employed. In figure 14 the best agreement between LES and DNS is achieved for $C_S = C_S^*/2$ which suggests that this choice of the Smagorinsky constant might be more appropriate than the optimized value C_S^*. Note, however, that for $C_S = C_S^*/2$ the integrated dissipation due to the SGS model accounts for merely a quarter of the correct one, owing to the fact that the modelled subgrid stresses (26) are proportional to C_S^2. For a conclusive assessment of the influence of C_S it is necessary to consider the resulting GS turbulent fluctuations in addition to the mean-velocity profiles. In figure 15 the averaged GS turbulent kinetic energy E_t^{GS},

$$\langle E_t^{GS} \rangle = \tfrac{1}{2} \langle \tilde{\bar{u}}_k \, \tilde{\bar{u}}_k \rangle = \langle E^{GS} \rangle - \tfrac{1}{2} \langle \bar{u}_k \rangle \, \langle \bar{u}_k \rangle , \tag{29}$$

is depicted for the three LES together with filtered and unfiltered DNS results. To allow a direct quantitative comparison, the bulk velocity u_Q (being the same for all LES and the DNS) has been chosen as reference velocity here. It is observed that for $C_S = 0$ and $C_S = C_S^*/2$ the GS turbulent kinetic energy is considerably in excess of the filtered DNS results, which illustrates the insufficient damping of the large-scale turbulence in these cases.

In figure 15 $C_S = C_S^*$ yields the best agreement between LES and filtered DNS, but a direct relation between this agreement and the optimization (28) cannot be

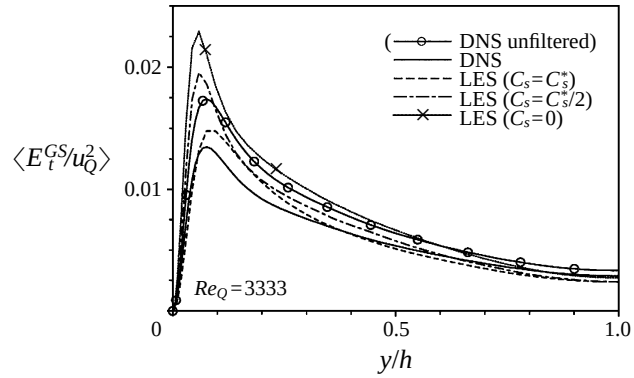

FIGURE 15. Averaged turbulence energy E_t^{GS} of the grid-scale motions normalized by the square of the bulk velocity u_Q. Comparison of DNS results (simulation II) with LES results for various values of the Smagorinsky constant C_S.

inferred. Since the production of turbulent kinetic energy directly depends on the mean-flow gradients, the errors in the mean-velocity profile (see figure 14) strongly affect the entire energy budget of the GS turbulence. The satisfactory performance of the Smagorinsky model for $C_S = C_S^*$ may hence be a mere coincidence. Figures 14 and 15 show that the Smagorinsky constant cannot be optimized in such a way that good results are achieved with respect to both mean-velocity profiles and turbulent fluctuations.

A remark may be in order here concerning the comparison of LES results with unfiltered and filtered DNS data. The unfiltered turbulent kinetic energy of SII was included in figure 15 for comparison. It is seen that the LES results for $C_S = C_S^*/2$ are in much better agreement with these data than with the filtered ones. If a comparison is based on unfiltered data from simulations or experiments, $C_S \approx 0.5\, C_S^*$ may appear to be the optimum choice for the Smagorinsky constant, giving a satisfactory agreement concerning the mean-velocity profile and the turbulence intensities. However, figure 15 reveals that a considerable amount of energy resides within the SGS motions in the near-wall flow, which makes clear that conclusive results can only be obtained if a comparison is based on appropriately filtered reference results. The use of unfiltered data, on the other hand, may lead to erroneous conjectures about the model performance in the near-wall flow.

The findings for $Re_Q = 3333$ may be generalized for the other bulk Reynolds numbers considered here. This is illustrated by figure 16, where the relative error $\Delta\tau_w$ in the wall stress,

$$\Delta\tau_w = \frac{\tau_{w,LES} - \tau_{w,DNS}}{\tau_{w,DNS}} = \frac{Re_{\tau,LES}^2 - Re_{\tau,DNS}^2}{Re_{\tau,DNS}^2}, \tag{30}$$

is plotted as a function of C_S for all LES we performed. Note that the averaged wall stress is directly related to the driving pressure gradient and is hence one of the most interesting integral quantities of the flow. In figure 16 the Smagorinsky constant is given in normalized form C_S/C_S^* on the abscissa. The suitability of this normalization, and hence the significance of C_S^*, becomes evident from the fact that the curves for the different Reynolds numbers almost collapse. The *a priori* test already suggested that the near-wall errors of the LES should depend little on the Reynolds number, which is now fully confirmed by figure 16.

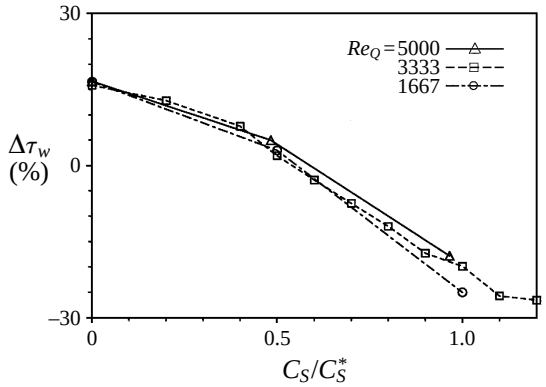

FIGURE 16. Relative error $\Delta\tau_w$ in the resulting wall shear stress of the LES as a function of the normalized Smagorinsky constant C_S/C_S^*. Results for LES at three different bulk Reynolds numbers Re_Q.

The results in figure 16 reveal that concerning τ_w the best results are generally obtained with $C_S \approx 0.5\,C_S^*$. If no model is applied ($C_S = 0$), the computed wall stress is too large by approximately $+15\%$, while an error of about -20% is observed for values of C_S close to C_S^*. The present results may be compared with results from Piomelli *et al.* (1988) who considered turbulent channel flow at a wall Reynolds number of about $Re_\tau = 180$. The authors reported a difference of -18% in the friction coefficient $c_f = 2\,\tau_w/u_Q^2$ between a DNS and a LES in which a cutoff filter and a Smagorinsky model with a constant of $C_S = 0.1$ were applied. In contrast to our study where the same mass flux is prescribed in both DNS and LES, Piomelli *et al.* (1988) conducted their direct and large-eddy simulations for the same wall Reynolds number Re_τ. However, the difference in wall friction between the LES and a DNS with the identical mass flux may be estimated from their results with the aid of the relation $Re_\tau \propto Re_Q^{7/8}$ (Dean 1978). This gives an error of slightly more than $\Delta\tau_w = -20\%$ which is in excellent agreement with our findings.

The present analysis was made for the Smagorinsky model only, but we expect that the findings may essentially be generalized to similar eddy-viscosity models. For example, Germano *et al.* (1991) compared the dynamic model with the Smagorinsky model for a channel flow at $Re_{CL} = 6100$, but regarding the mean-velocity profiles or the turbulence intensities no significant differences between the two models were found. More recently Horiuti (1993) examined different SGS models, among them the Smagorinsky model and a new model which will briefly be introduced in the next section. Among other things, Horiuti compared LES and DNS results of turbulent channel flow at $Re_\tau = 390$. Consistent with the present findings, all LES showed a good agreement with the DNS data concerning the mean-velocity profile, but the turbulence intensities were clearly too high.

6. An improved definition of the SGS eddy viscosity

The eddy-viscosity ansatz is a particularly convenient approach to model the subgrid stresses and has become most common in LES. Therefore it is of interest to clarify whether the shortcomings of current SGS models, which were discussed in the preceding section, are inherent in the eddy-viscosity ansatz. To this end we will compare three definitions of the eddy viscosity in this section, which differ with

respect to the characteristic scales used. In the present comparison these characteristic scales are taken from DNS results (SII) directly which keeps the investigation free of further modelling assumptions. This, however, implies that the respective eddy viscosities cannot directly be utilized in a LES. For simplicity we will still denote them as 'models' in this section. In order to derive applicable subgrid models from the eddy viscosities examined here, one might resort to an approximate evaluation of the characteristic scales with the aid of a scale-similarity assumption (see Horiuti 1993) or some test filtering similar to that employed in the dynamic Smagorinsky model. In this section we will apply the same filter widths that were used in the analysis of the energy budget in §4 (see table 2).

To evaluate the eddy viscosity ν_t in (24), two characteristic scales of the SGS turbulence need to be specified. For example, a time scale T and a (quadratic) velocity scale E can be employed:

$$\nu_t \propto T \cdot E. \tag{31}$$

In general, the selection of the most appropriate characteristic scales is no trivial task and may strongly depend on the actual flow. In LES it is common to relate E to the SGS kinetic energy $E^{SGS} = (u'_k u'_k)/2$, while the grid size Δx is taken as a characteristic length scale L (which corresponds to setting $T = \Delta x/E^{1/2}$). This definition of the eddy viscosity was studied e.g. by McMillan & Ferziger (1979) who analysed homogeneous isotropic turbulence. For wall-bounded flows one should supply an additional damping function $D(y^+)$ to ensure the proper near-wall limiting behavior $\nu_t \propto (y^+)^3$. The resulting eddy viscosity, referred to as 'model A' hereafter, reads

$$\nu_t = D(y^+)\, C_A\, \Delta x (\, u'_k u'_k)^{1/2}, \quad D(y^+) = 1 - \exp(-(y^+/25)^2), \tag{32}$$

where $\Delta x = (\Delta x_1 \Delta x_2 \Delta x_3)^{1/3}$. In (32) C_A denotes a yet undetermined constant. For homogeneous isotropic turbulence C_A can be derived analytically which yields (see Härtel 1994)

$$C_A = \frac{1}{\pi}\left(\frac{2}{3\alpha}\right)^{3/2}, \tag{33}$$

where α denotes the Kolmogorov constant. In more general cases the constant needs to be determined empirically according to some additional condition. We applied the optimization (28) here which yields a value of $C_A = 0.073$ for $Re_\tau = 210$ and the given filter widths.

Horiuti (1993) suggested an alternative definition of the eddy viscosity, where E is evaluated using the wall-normal SGS velocity only, i.e. where $(u'_3 u'_3)/2$ is employed to evaluate E rather than $(u'_k u'_k)/2$. This model, named 'model B' in this section, utilizes the quadratic damping of the normal velocity component close to the wall, thus avoiding additional empirical near-wall corrections. The complete definition of the eddy viscosity reads

$$\nu_t = C_B\, \Delta x \frac{u'_3 u'_3}{(u'_k u'_k)^{1/2}}. \tag{34}$$

Like for model A, Δx is computed as $\Delta x = (\Delta x_1 \Delta x_2 \Delta x_3)^{1/3}$. The constant C_B in (34) can be determined from the normalization (28) which gives a value of $C_B = 0.197$ in the present case.

The analysis in §4 confirms that close to the wall the normal component of the SGS kinetic energy provides a better velocity scale than the total SGS kinetic energy. This holds not only with respect to the near-wall damping of the turbulence, but

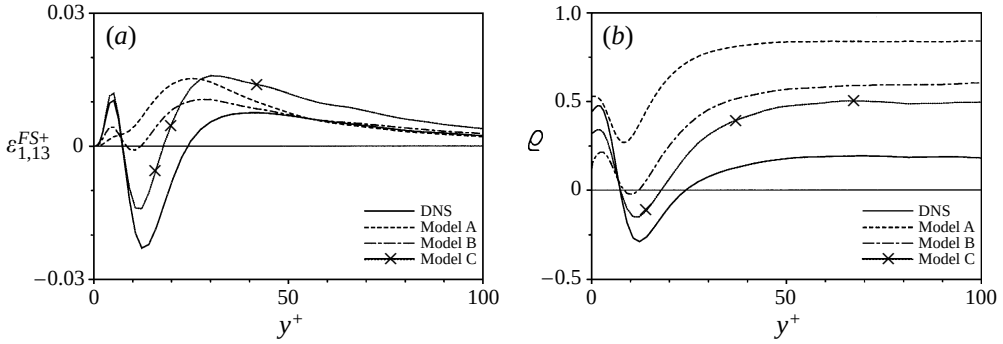

FIGURE 17. (*a*) Contribution of the SGS stress component Q_{13} to ε_1^{FS}. (*b*) Correlation coefficient between $\tilde{\tau}_{13}$ and $\tilde{\bar{S}}_{13}$. Comparison of DNS data and *a priori* results for various SGS models. Results for simulation II.

also with respect to subtle details of the interactions between GS and SGS motions. Figures 7 and 9 suggest that τ_{13} should directly be set proportional to $Q_{33}\,\partial\bar{u}_1/\partial x_3$. This is equivalent to setting τ_{13} proportional to $Q_{33}\,\bar{S}_{13}$, because from our analysis we found that the gradient $\partial\bar{u}_3/\partial x_1$ plays only a marginal role. Since the respective results in §4 were given in wall units, this implies that the time scale T is set equal to the viscous time scale $t_w = \nu/u_\tau^2$ of the wall layer. Consequently, the eddy viscosity should be computed as

$$\nu_t = -C_C \frac{Q_{33}}{u_\tau^2}\nu. \tag{35}$$

The above definition will be called 'model C' in the remainder of the paper. From the normalization (28) a value of $C_C = 6.42$ is computed for the model constant. In model C the limiting behaviour of ν_t is $\propto (y^+)^4$ rather than $\propto (y^+)^3$, but no attempt to correct this slight discrepancy is made here.

At first sight it might be surprising that, in contrast to the other models outlined above, the grid size does not enter the eddy viscosity (35), which makes ν_t a function of one characteristic SGS quantity (Q_{33}) only instead of two. This, however, is not inconsistent with the physical properties of near-wall turbulence. Since the wall layer tends to establish a universal behaviour if scaled in wall units, all quantities like averaged velocity profiles or energy spectra collapse in non-dimensional form. This implies that for a given dimensionless grid size Δx^+ the corresponding dimensionless SGS stress Q_{33}^+ is uniquely determined and vice versa. Hence only one degree of freedom is left on which the SGS eddy viscosity may depend, if the problem is recast in wall units. It must be stressed, however, that (35) can only be physically meaningful in the wall region, since the universal scaling using ν and u_τ has no significance within the outer flow.

6.1. A-priori *test of the models*

The three models outlined above were examined in an *a priori* test using the database of SII. Figure 17 gives the results for $\varepsilon_{1,13}^{FS}$ obtained from the DNS data and models A, B, and C, respectively. It is readily seen that the pronounced negative minimum within the buffer layer is only captured satisfactorily with the new formulation C, although a global, weakly negative minimum is observed for model B as well. For model A the quantity $\varepsilon_{1,13}^{FS}$ is non-negative throughout and does not exhibit the characteristic

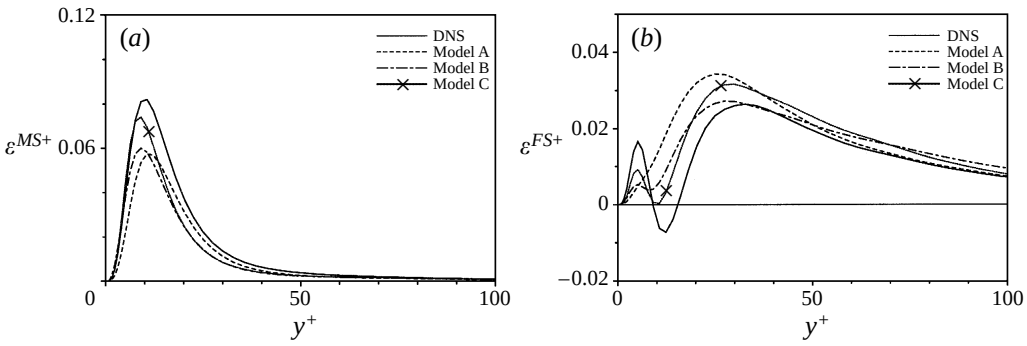

FIGURE 18. SGS dissipation ε^{MS} due to mean rates of strain (*a*) and ε^{FS} due to fluctuating rates of strain (*b*). Comparison of DNS results with various SGS models. Results for simulation II.

minimum. It may hence be concluded that the definition A of the eddy viscosity is not suited for an adequate SGS modelling in near-wall turbulence.

It must be emphasized that the above conclusion concerning model A is not in contradiction with figure 10, where a negative correlation between all $\tilde{Q}_{ii}$ (no summation) and $\tilde{\bar{S}}_{13}$ was found. From that result one might have suspected that incorporating the SGS energy into the eddy viscosity provides the desired negative correlation between $\tilde{\bar{S}}_{13}$ and $\tilde{\tau}_{13}^{mod}$. However, the correlation coefficients between $\tilde{\bar{S}}_{13}$ and $\tilde{\tau}_{13}^{mod}$ shown in figure 17 reveal that model A exhibits a high positive correlation throughout. This is due to the fact that in (32) the square root of E^{SGS} enters, rather than E^{SGS}, which results in considerably altered phase relations and correlation coefficients.

To provide a more global comparison of the various models, results for ε^{MS} and ε^{FS} are displayed in figure 18. Note that the model coefficients have been adjusted such that $\varepsilon^{FS} + \varepsilon^{MS}$, integrated over the whole channel, is identical with the DNS value as a consequence of (28). Figure 18 again confirms that model C performs best in the near-wall region. Although a kink in the curve for ε^{FS} is also found for model B, it is much more pronounced for model C. In the curve for model A such a kink is not discernible at all, as was to be expected from the results shown in figure 17.

The above results for model C indicate that the inverse cascade of kinetic energy in the buffer layer may in principle be accounted for by an eddy-viscosity ansatz. Moreover it becomes clear that the performance of eddy-viscosity models in the near-wall region crucially depends on the proper choice of the characteristic scales. Clearly, model C, which was derived from the present analysis of the turbulent energy budget, is valid in the near-wall region only, and cannot be applied in the outer layer of a wall-bounded flow at high Reynolds number. Consequently, an SGS model based on the form C of the eddy viscosity would have to be coupled with a common subgrid model for the outer flow in an actual LES. This suggests that subgrid models employed in complex flows may have to be adjusted to the various flow regimes in a very substantial way.

7. Concluding remarks

In the present paper a detailed numerical study is presented which aims at clarifying several issues relevant to the large-eddy simulation of wall-bounded turbulence. The study contains (i) a thorough analysis of the turbulent energy budget in the near-wall

flow, (ii) *a priori* and *a posteriori* tests of current subgrid models, and (iii) a more fundamental examination of the eddy-viscosity ansatz.

The analysis of the energy budget focused on the inverse cascade of kinetic energy within the buffer layer already described in a previous paper (Härtel *et al.* 1994). The analysis was primarily based on DNS data of turbulent channel flow at a wall Reynolds number of $Re_\tau = 210$. To assess the Reynolds-number dependence of the results, two further direct simulations at $Re_\tau = 115$ and $Re_\tau = 300$ were conducted and analysed. A significant Reynolds-number dependence could not be observed. The analysis reveals that the inverse transfer of kinetic energy almost exclusively affects the energy budget of the streamwise GS velocity, and that it is due to the SGS stress aligned with the mean rate of strain. To examine the contribution of this stress component to the energy transfer in more detail, the individual terms in the respective transport equation were evaluated. It turned out that the correlation of the wall-normal SGS stress and the wall-normal derivative of the streamwise GS velocity plays the decisive role in the occurrence of the inverse cascade.

The *a priori* test of three more widely utilized SGS models showed that none of them is able to account for the inverse energy cascade. One of the models, the classical Smagorinsky model, was employed in a series of LES of turbulent channel flow at different Reynolds numbers. The results of these simulations feature significant errors in the near-wall region as was to be expected from the previous *a priori* test. We assume that these errors are mainly caused by the deficiencies of the model in the buffer layer. Consistent with what was found in the *a priori* test and in the analysis of the energy budget, the key features of the LES results in the near-wall region appear to be essentially unaffected by the Reynolds number. This is true despite the fact that the LES results in the core flow improve significantly with increasing Reynolds number. Concerning the comparison of LES data with unfiltered and filtered reference data, it was pointed out that conclusive results can only be obtained with the latter.

Motivated by the observed deficiencies of the eddy-viscosity models, the eddy-viscosity ansatz was examined in a more fundamental manner. Three definitions of the eddy viscosity were investigated which differ with respect to the characteristic scales employed. For all three models DNS data were used to evaluate these scales, which kept the study clear of additional modelling assumptions. Two of the definitions were previously suggested in the literature, while the third one was derived directly from the present analysis of the near-wall energy budget. Only the latter definition was found to give satisfactory results in the near-wall region, which shows that the proper choice of the characteristic scales is of utmost importance for the subgrid modelling in this flow regime. Since the newly derived eddy viscosity can be applied in the near-wall flow only, a possible new subgrid model based on this definition of the eddy viscosity would have to be coupled with a 'common' subgrid model for the outer flow. An important finding is that the inverse cascade of energy may in principle be accounted for by an eddy-viscosity ansatz.

The present analysis is confined to flows at moderate Reynolds numbers where DNS data are available. However, since the results did not exhibit an appreciable Reynolds-number dependence, we assume that the findings may essentially be generalized to flows at higher Reynolds numbers which are of more practical interest. It should be emphasized that the rather small filter widths employed in the present study may hardly be affordable in practical applications. Since larger filter widths enhance the inverse energy cascade, model deficiencies in the near-wall flow may then become much more severe. In the present paper no improved subgrid model was presented which can directly be applied in a LES, but a possible line of development is indicated

by the new form of the eddy viscosity. The respective characteristic scales, which were directly taken from the DNS results here, may be obtained in an approximate manner by some test filtering similar to that one employed in the dynamic Smagorinsky model.

Part of this work has been supported by the Deutsche Forschungsgemeinschaft.

REFERENCES

Antonia, R. A. & Kim, J. 1994 Low-Reynolds-number effects on near-wall turbulence. *J. Fluid Mech.* **276**, 61–80.

Balaras, E. & Benocci, C. 1994 Subgrid scale models in finite difference simulations of complex wall bounded flows. In *Application of Direct and Large Eddy Simulation to Transition and Turbulence, AGARD-CP*-551.

Canuto, C., Hussaini, M. Y., Quarteroni, A. & Zang, T. A. 1988 *Spectral Methods in Fluid Dynamics*. Springer.

Chollet, J.-P. & Lesieur, M. 1981 Parameterization of small scales of three-dimensional isotropic turbulence utilizing spectral closures. *J. Atmos. Sci.* **38**, 2747–2757.

Clark, R. A., Ferziger, J. H. & Reynolds, W. C. 1979 Evaluation of subgrid-scale models using a fully simulated turbulent flow. *J. Fluid Mech.* **91**, 1–16.

Comte, P., Lee, S. & Cabot, W. H. 1990 A subgrid-scale model based on the second-order velocity structure function. In *Proc. 1990 Summer Program, Center for Turbulence Research*, pp. 31–45.

Dean, R. B. 1978 Reynolds number dependence of skin friction and other bulk flow variables in two-dimensional rectangular duct flow. *Trans. ASME*: *J. Fluids Engng* **100**, 215–223.

Deardorff, J. W. 1970 A numerical study of three-dimensional turbulent channel flow at large Reynolds numbers. *J. Fluid Mech.* **41**, 453–480.

Domaradzki, J. A., Liu, W., Härtel, C. & Kleiser, L. 1994 Energy transfer in numerically simulated wall-bounded turbulent flows. *Phys. Fluids* **6**, 1583–1599.

Domaradzki, J. A., Rogallo, R. S. & Wray, A. A. 1990 Interscale energy transfer in numerically simulated turbulence. In *Proc. 1990 Summer Program, Center for Turbulence Research*, pp. 319–329.

Galperin, B. & Orszag, S. A. (Eds.) 1993 *Large Eddy Simulation of Complex Engineering and Geophysical Flows*. Cambridge University Press.

Germano, M., Piomelli, U., Moin, P. & Cabot, W. H. 1991 A dynamic subgrid-scale eddy viscosity model. *Phys. Fluids* A **3**, 1760–1765.

Ghosal, S., Lund, T. S., Moin, P. & Akselvoll, K. 1995 A dynamic localization model for large-eddy simulation of turbulent flows. *J. Fluid Mech.* **286**, 229–255.

Gilbert, N. & Kleiser, L. 1991 Turbulence model testing with the aid of direct numerical simulation results. In *Proc. 8th Symp. on Turbulent Shear Flows, Munich, September 9–11.*

Härtel, C. 1994 Analyse und Modellierung der Feinstruktur im wandnahen Bereich turbulenter Scherströmungen. Doctoral Dissertation, Technical University of Munich. Also: DLR-FB 94–22, Deutsche Forschungsanstalt für Luft- und Raumfahrt, Germany.

Härtel, C. 1996 Turbulent flows: direct numerical simulation and large-eddy simulation. In *Handbook of Computational Fluid Mechanics* (ed. R. Peyret). Academic.

Härtel, C. & Kleiser, L. 1997 Galilean invariance and filtering dependence of near-wall grid-scale/subgrid-scale interactions in large-eddy simulation. *Phys. Fluids* **9**, 473–475.

Härtel, C., Kleiser, L., Unger, F. & Friedrich, R. 1994 Subgrid-scale energy transfer in the near-wall region of turbulent flows. *Phys. Fluids* **6**, 3130–3143.

Horiuti, K. 1993 A proper velocity scale for modelling subgrid-scale eddy viscosities in large eddy simulation. *Phys. Fluids* A **5**, 146–157.

Kleiser, L. & Schumann, U. 1984 Spectral simulations of the laminar-turbulent transition process in plane Poiseuille flow. In *Spectral Methods for Partial Differential Equations* (ed. R. G. Voigt, D. Gottlieb & M. Y. Hussaini), pp. 141–163. SIAM.

Leonard, A. 1974 Energy cascade in large-eddy simulations of turbulent fluid flows. *Adv. Geophys.* A **18**, 237–248.

Lilly, D. K. 1967 The representation of small-scale turbulence in numerical simulation experiments. In *Proc. IBM Scientific Computing Symp. on Environmental Sciences, Thomas J. Watson*

Res.Center, Yorktown Heights, NY, pp. 195–210. IBM Form 320–1951.

Lilly, D. K. 1992 A proposed modification of the Germano subgrid-scale closure method. *Phys. Fluids* A **4**, 633–635.

McMillan, O. J. & Ferziger, J. H. 1979 Direct testing of subgrid scale models. *AIAA J.* **17**, 1340–1346.

Métais, O. & Lesieur, M. 1992 Spectral large-eddy simulation of isotropic and stably-stratified turbulence. *J. Fluid Mech.* **239**, 157–194.

Piomelli, U. 1993 High Reynolds number calculations using the dynamic subgrid-scale stress model. *Phys. Fluids* A **5**, 1484–1490.

Piomelli, U., Cabot, W. H., Moin, P. & Lee, S. 1991 Subgrid-scale backscatter in transitional and turbulent flows. *Phys. Fluids* A **3**, 1766–1771.

Piomelli, U., Ferziger, J. H. & Moin, P. 1989 New approximate boundary conditions for large-eddy simulations of wall-bounded flows. *Phys. Fluids* A **1**, 1061–1068.

Piomelli, U., Moin, P. & Ferziger, J. H. 1988 Model consistency in large-eddy simulation of turbulent channel flow. *Phys. Fluids* **31**, 1884–1891.

Rogallo, R. S. & Moin, P. 1984 Numerical simulation of turbulent flows. *Ann. Rev. Fluid Mech.* **16**, 99–137.

Schumann, U. 1975 Subgrid scale model for finite difference simulation of turbulent flows in plane channels and annuli. *J. Comput. Phys.* **18**, 376–404.

Schumann, U. 1991 Introduction to the modelling of turbulence. *VKI Lecture Series 1991-02, Von Karman Institute for Fluid Mechanics, Rhode–Saint–Genèse, Belgium.*

Smagorinsky, J. 1963 General circulation experiments with the primitive equations. I. The basic experiment. *Mon. Weath. Rev.* **91**, 99–164.

Van Driest, E. R. 1956 On the turbulent flow near a wall. *J. Aero. Sci.* **23**, 1007–1011.

Wei, T. & Willmarth, W. W. 1989 Reynolds-number effects on the structure of a turbulent channel flow. *J. Fluid Mech.* **204**, 57–95.

Zang, T. A. 1991 Numerical simulation of the dynamics of turbulent boundary layers: Perspectives of a transition simulator. *Phil. Trans. R. Soc. Lond.* A **336**, 95–102.

Zang, T. A., Chang, C.-L. & Ng, L. L. 1992 The transition prediction toolkit: LST, SIT, PSE, DNS and LES. In *Proc. Fifth Symp. on Numerical and Physical Aspects of Aerodynamic Flows, Long Beach, January 13–15.*